energies

MDPI

Article

Effects of Packer Locations on Downhole Electric Heater Performance: Experimental Test and Economic Analysis

Wei Guo [1,2,3], Zhendong Wang [1,2,3,*], Youhong Sun [2,3,4], Xiaoshu Lü [1,2,5,6], Yuan Wang [1,2,3], Sunhua Deng [1,2,3] and Qiang Li [1,2,3,*]

1 College of Construction Engineering, Jilin University, Changchun 130021, China; guowei6981@jlu.edu.cn (W.G.); xiaoshu.lu@aalto.fi (X.L.); wy2019@jlu.edu.cn (Y.W.); dengsh@jlu.edu.cn (S.D.)
2 National-Local Joint Engineering Laboratory of In-situ Conversion, Drilling and Exploitation Technology for Oil Shale, Jilin University, Changchun 130021, China; syh@jlu.edu.cn
3 Key Lab of Ministry of Natural Resources for Drilling and Exploitation Technology in Complex Conditions, Jilin University, Changchun 130021, China
4 China University of Geosciences, Beijing 100083, China
5 Department of Electrical Engineering and Energy Technology, University of Vaasa, FIN-65200 Vaasa, Finland
6 Department of Civil and Structural Engineering, School of Engineering, Aalto University, P.O. Box 12100, FIN-02015 Espoo, Finland
* Correspondence: zhendong18@mails.jlu.edu.cn (Z.W.); lqiang1982@jlu.edu.cn (Q.L.)

Received: 8 November 2019; Accepted: 7 January 2020; Published: 13 January 2020

Abstract: A downhole electric heater, which reduces heat loss along a heat insulation pipe, is a key apparatus used to ignite oil shale underground. Downhole heaters working together with packers can improve the heating efficiency of high-temperature gases, while different packer locations will directly affect the external air temperature of the heater shell and, subsequently, the performance and total cost of the downhole heaters. A device was developed to simulate the external conditions of heater shells at different packer locations. Then, the effects of external air temperature on the performance of a downhole heater with pitches of 50, 160, and 210 mm were experimentally studied. In the test, results indicated that the heater with a packer at its outlet had an accelerated heating rate in the initial stage and decreased temperature in the final stage. Additionally, the lowest heating rod surface temperature and highest comprehensive performance were achieved with minimal irreversible loss and lower total cost when using a downhole electric heater with a packer set at its outlet. In addition, the downhole electric heater with a helical pitch of 50 mm and a packer at its outlet was more effective than other schemes in the high Reynolds number region. These findings are beneficial for shortening the oil production time in oil shale in situ pyrolysis and heavy oil thermal recovery.

Keywords: oil shale; in situ pyrolysis; packer; downhole electric heater; economic analysis

1. Introduction

With the continuous exploitation of conventional oil reservoirs, easy-to-exploit light oil is dramatically reduced. Unconventional oil reservoirs, such as heavy oil and oil shale, are the main driving forces for future oilfield production [1–3]. Heavy oil and super-heavy oil can be utilized after reducing their viscosity. Moreover, oil shale is an immature source rock that needs to be heat treated to convert kerogen into oil and gas [2–4]. At present, oil shale in situ pyrolysis is the mainstream technology used for oil shale exploitation [5–7]. From the perspective of heat transfer, the heat transfer process during heat carrier (superheated steam, nitrogen) injection in steam huff and puff, steam

flooding, and oil shale in situ pyrolysis is similar [7–9]. Superheated steam or nitrogen is produced on the ground, and then injected into reservoirs via heat insulation pipe [6–9]. Therefore, techniques or conclusions found in oil shale in situ pyrolysis can be applied to steam huff and puff, and steam flooding. In the National Pilot Project for Oil Shale in situ Exploitation of China (NPOSE) [5], shortcomings of the high-temperature nitrogen injection method were found: (1) nitrogen had a large heat loss along the heat insulation pipe, and (2) the casings and heat insulation pipe were prone to deformation or buckling.

To reduce the heat loss along heat insulation pipes, Guo [9] developed a downhole electric heater with continuous helical baffles (DEHCHB) to place high-temperature heat carrier (air) generators underground. The deeper the oil shale or heavy oil is buried, the more obvious the advantages of the DEHCHB. Guo [9] explored the shell-side flow and temperature field of the downhole electric heater with segmental baffles and continuous helical baffles. Compared with the heater with segmental baffles, the regular spiral flow of DEHCHB was found to help to reduce the tube vibrations of the tube bundle and was helpful in the uniform distribution of the electric heating rod surface temperature.

In oil shale in-situ pyrolysis, downhole electric heaters are mainly used to ignite oil shale. To rapidly ignite oil shale, it is necessary to heat the oil shale block intensively, which requires the downhole electric heater and packer to work together. In addition, the hot and cold convection of air in the heating well can be effectively prevented by setting the packer, which not only reduces thermal damage to the casing and heat insulation pipe, but also improves the energy injection efficiency of the heat carrier, shortening the oil production time. Furthermore, the location of the packer directly affects the external air temperature of the heater shell and, subsequently, the heat transfer and resistance performance of the downhole heater. When the packer is placed at the heater outlet (Figure 1), the annulus between the downhole heater and the heating well is filled with cold air, and the heat is transferred from the heater shell to the cold air. When the packer is placed at the heater inlet (Figure 2), the annulus is filled with hot air, and hot air transfers heat to the shell-side air through the heater shell and to oil shale formation through the heating well. A heat transfer schematic diagram of the two schemes is presented in Figure 1.

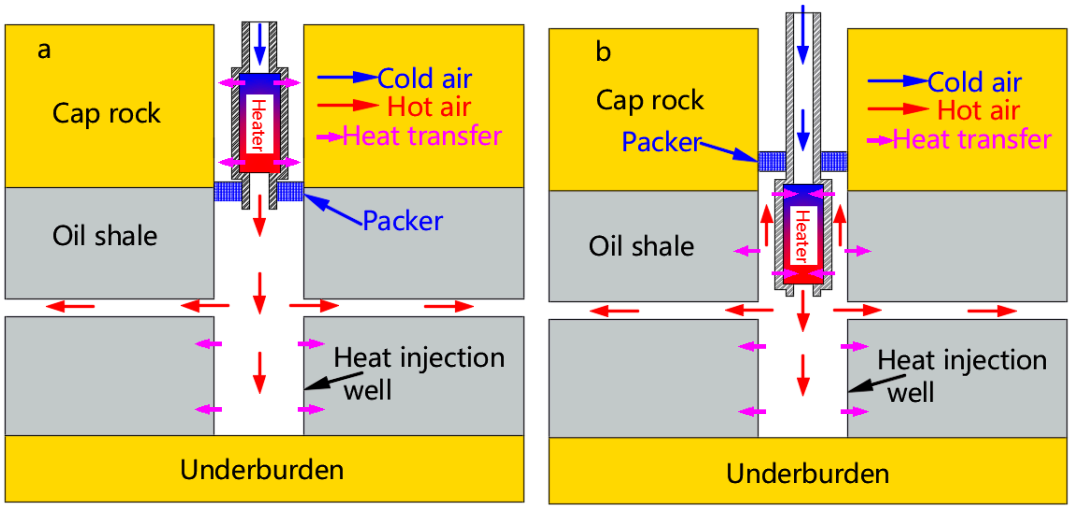

Figure 1. Heat transfer schematic diagram of (**a**) Figure 1 and (**b**) Figure 2.

Many scholars have focused on studying the effects of different heat transfer structures on the performance of heat exchangers, and seldom consider the influence of the external air temperature of the heat exchanger shell on heat exchanger performance. Du [10] investigated continuous helical baffled heat exchangers with different arrangements in inclination angle of the elliptical tube, by using numerical simulation. They found that an elliptical tube can dramatically increase the comprehensive performance when the shell-side Reynolds number is relatively small. Yadav [11] studied the effect of

helical surface disc turbulators on the performance of double-pipe heat exchangers and discovered that a heat exchanger with smaller pitch and diameter had the highest performance. Gu [12] numerically and experimentally investigated the performance of a heat exchanger with a trapezoidal baffle. They discovered that the thermal performance factor (TPF) of the trapezoidal baffle heat exchanger increased by 14.9–19.2%, when compared to a shutter baffle heat exchanger. Wang [13] numerically studied a double-shell-side rod baffle heat exchanger and observed that the comprehensive performance of the heat exchanger was higher than the single one, with a maximum of 8.9%. In previous research, because downhole heaters working with packers was newly discovered in oil exploitation heating technology, little consideration was given to the effects of the external conditions of the downhole heater shell on its performance. Therefore, this needs to be carefully studied to provide a reliable basis for the design of downhole heaters and the setting of heating parameters in oil exploitation.

This paper attempts to provide a more detailed investigation into the effects of external air temperature of the heater shell, on downhole heater performance. In this study, newly developed devices were used to simulate the external conditions of heater shells at different packer locations. Finally, the outlet temperature response characteristics, comprehensive performance, total cost, and irreversible loss of a downhole heater with different pitch values under two schemes, were experimentally explored.

2. Experimental Setup

2.1. Experimental Apparatus

Except for the different pitches of the continuous helical baffle, the remaining parameters of the tested heater in the same scheme were identical. The inner and outer diameters of the heater shell were 131 mm and 139 mm, and those of the casing were 205.7 mm and 219.1 mm, respectively. The effective geometry (outer diameter × length) of the heating rod was 16 mm × 1000 mm, and the length of the casing was 1085 mm. Six heating rods were arranged in a uniform circular arrangement. In all tests, the heater was placed vertically, because downhole heaters are installed vertically in the heating well during oil exploitation. Figure 2 shows a schematic diagram of the tested device. The heat transfer structure of heaters is depicted in Figure 3.

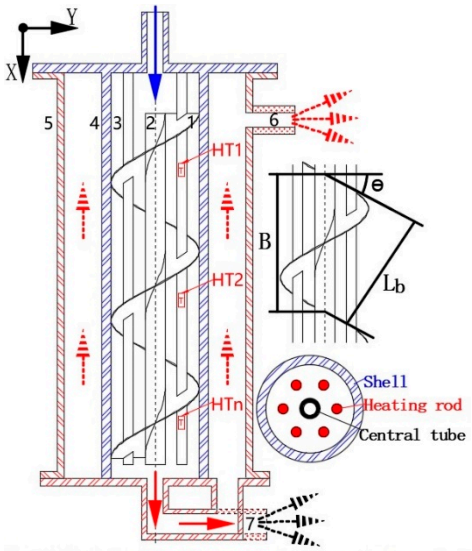

Figure 2. Schematic diagram of the tested device.

Figure 3. Heat transfer structure of heaters.

2.2. Experiment System

In this work, the experiments were conducted on three DEHCHBs, with pitches of 50, 160, and 210 mm. Figure 4 shows a schematic diagram and photograph of the experimental system. The experimental system consisted of three separate parts: compressed air supply, electronic control, and data collection systems. The compressor provided compressed air, then the oil and water in compressed air were filtered through a tertiary filter, before being injected into the heater. The electronic control system controls the opening and closing, and heating power of the heater. Turning the heater on and off was controlled by the temperature control meter. Heating power was controlled by a power regulator. Temperature and pressure data were collected by a paperless recorder.

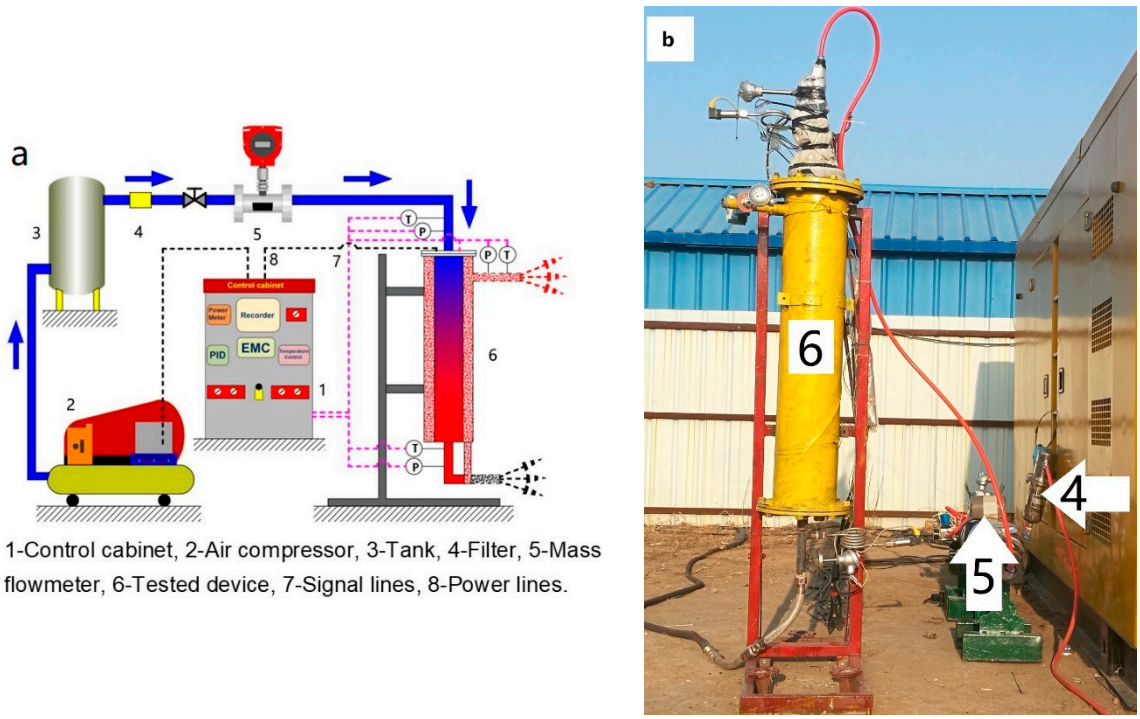

Figure 4. (**a**) Schematic diagram and (**b**) photograph of experimental system.

Two kinds of temperature sensors were applied in the experiments: platinum resistance thermometers (PT100) were positioned at the inlet and outlet of the downhole heater and casing, and K-type thermocouples were attached to the electric heating rod surface (covering different temperature ranges). The shell-side resistance was measured via capacitive differential pressure sensors. Table 1 shows the parameters of the temperature sensors.

Table 1. Parameters of heating rod temperature sensors.

Heater	Pitch (mm)	Locations on Heating Rod Along X Axis (mm)
H50	50	50, 190, 390, 590, 790, 990
H160	160	150, 310, 470, 630, 790, 950
H210	210	120, 330, 540, 750, 960

Here, H represents heater with helical baffles, and 50, 160, and 210 represent helical pitch values.

2.3. Test Scheme

The DEHCHB and casing outlets were set with a free-flow condition. There were two experimental schemes. In Figure 1, the packer was placed at the heater outlet; and in Figure 2, the packer was placed at the heater inlet.

Each scheme was conducted under two experimental conditions: constant heating power and constant outlet temperature. In the constant heating power scheme, each heater was used to analyze outlet temperature response characteristics, heat transfer performance, resistance performance, and economic analysis, with five mass flow rates and three power values.

The heating rod surface temperature distribution trend was explored in the constant outlet temperature scheme, in which the mass flow rate of air (M_s) was 0.017 kg/s and air outlet temperature (t_{out}) was 270 °C.

2.4. Data Processing

2.4.1. Heat Transfer Equations

Few studies have examined downhole electric heaters. The shell-side air-flow pattern and heat transfer structure of downhole heaters are similar to shell-and-tube heat exchangers. By changing the heat transfer rate and heat transfer temperature difference, the overall heat transfer coefficient of the downhole heater is obtained.

The overall heat transfer coefficient (h.t.c.) (K) of the heater is [14]:

$$K = \frac{P_e}{A\Delta t_m} \tag{1}$$

The effective power is:

$$P_e = (f_{out} - f_{in})M_s \tag{2}$$

$$\Delta t_m = \frac{\Delta t_{max} - \Delta t_{min}}{ln\frac{\Delta t_{max}}{\Delta t_{min}}} \tag{3}$$

$$\Delta t_{max} = T_{1050} - T_{out} \tag{4}$$

$$\Delta t_{min} = T_{50} - T_{in} \tag{5}$$

where f_{out} is the enthalpy of air at the outlet of the heater, f_{in} is the enthalpy of air at the inlet of heater, M_s is the mass flow rate of air, T_{1050} is the surface temperature of the heating rod at 1050 mm, T_{50} is the surface temperature of the heating rod at 50 mm, and t_{in} and t_{out} are the inlet and outlet air temperature, respectively.

The shell-side Reynolds number is expressed as follows:

$$R_e = \frac{d_e U_s \rho}{\mu} \tag{6}$$

The shell-side specific velocity (U_s) is:

$$U_s = \frac{M_s}{\rho A_{min}} \tag{7}$$

The minimal free-flow area (A_{min}) at the shell center line is expressed by the following equation [14]:

$$A_{min} = 0.5B \cos\theta (D_s - D_{lc} - 2d_{out}) \tag{8}$$

where B is the helical pitch, θ is the helix angle, D_s is the inner diameter of the heater shell, D_{lc} is the outer diameter of the central tube, and d_{out} is the outer diameter of the electric heating rod.

The convective heat transfer coefficient of the electric-heating rod is [15]:

$$h = \frac{\lambda N_u}{d_e} \tag{9}$$

The Nusselt number (N_u) is calculated as follows [16,17]:

$$N_u = C R_e^m P_r^{\frac{1}{3}} \tag{10}$$

The physical properties of air were evaluated using a polynomial expression with a degree of exactness, with the average inlet and outlet air temperatures as characteristic variables.

The heater thermal resistance is expressed as:

$$\frac{1}{K} = \frac{1}{h_s} + R_f \tag{11}$$

The fouling resistance (R_f) was not considered because the heaters were newly manufactured [18,19]. Thus, the following formula can be obtained:

$$K = h_s \tag{12}$$

The friction factor reflects the flow friction characteristic of the downhole heater [14]:

$$f = \frac{d_{out} \Delta p}{2\rho U_s^2} \tag{13}$$

The heat transfer factor is defined as follows [14]:

$$j = \frac{h_s}{\rho U_s c_p} (P_r)^{\frac{2}{3}} \tag{14}$$

2.4.2. Economic Analysis

The total cost (C_{tot}) of the downhole electric heater can be divided into initial cost (C_i) and total discounted operating cost (C_{tdo}):

$$C_{tot} = C_i + C_{tdo} \tag{15}$$

The initial cost (manufacturing cost) is the purchase cost of the downhole heater. For the heater shell and heating rod bundles, initial cost is based on the heat exchange area and manufacturing experience. This can be expressed as a function of heat exchange area, according to Hall's research [20].

The purchase cost of the downhole heater depends on the operating pressure, heater outlet temperature, and material cost. Initial cost is expressed in Equation (16) [20] (Table 2 lists the pressure and temperature factor):

$$C_i = \delta_M \delta_P \delta_T C_{pu} \tag{16}$$

where δ_M is the material factor, δ_M = 2.9.

Table 2. Pressure and temperature factor.

Design Pressure Value (Pa)	Pressure Factor δ_P	Design Temperature Value (°C)	Temperature Factor δ_T
1000	2.00	0–100	1.00
10,000	1.30	300	1.60
50,000–700,000	1.00	500	2.10

The purchase cost of the heater is obtained by using the following equation [21]:

$$C_{pu} = 500 + 324A^{0.91} \tag{17}$$

It should be noted that the downhole heater is made of 304 stainless steel, and the heating rod surface is smooth.

The total discounted operating cost is determined as [22]:

$$C_{tdo} = \sum_{i=1}^{ny} \frac{C_o}{(1+k)^i} \tag{18}$$

$$C_o = P_p C_e \tau \tag{19}$$

where C_o, ny, k, P_p, C_e, and τ, are annual operating cost, heater life cycle (year), annual discount rate (%), pumping power (W), the price of electrical energy (€/W·h), and hours of operation per year, respectively; ny = 10 years, k = 10%, $C_e = 1.2 \cdot 10^{-4}$, and τ = 330 days or 7902 h/year [23,24].

$$P_p = \frac{M_s \Delta P}{\eta} \tag{20}$$

where η is the pump efficiency, η = 0.7.

2.4.3. Second-Law Analysis Equations

From the perspective of thermodynamics, each heat transfer process is irreversible, and this irreversibility is evaluated by entropy generation. The entropy generation of the downhole electric heater is caused by airflow friction with finite pressure drops, and heat transfer with finite temperature differences [9].

The entropy generation resulting from airflow resistance can be written as follows [19]:

$$\dot{S}_{gen,\Delta p} = M_s \frac{\Delta p}{\rho} \frac{\ln(t_{out}/t_{in})}{t_{out} - t_{in}} \tag{21}$$

The entropy generation with finite temperature difference is calculated as [25]:

$$\dot{S}_{gen,\Delta t} = \int_{in}^{out} \left(\frac{M_s c_p d_t}{t} \right) = M_s c_p \ln\left(\frac{t_{out}}{t_{in}} \right) \tag{22}$$

The overall entropy generation rate of the downhole heater is presented as:

$$\dot{S}_{gen} = \dot{S}_{gen,\Delta p} + \dot{S}_{gen,\Delta t} \tag{23}$$

It has been discovered that the traditional entropy generation value in heaters with spiral flow may result in an entropy generation paradox. To make the calculation results more suitable for the

helical flow pattern of the downhole heater, the non-dimensional method for entropy generation rate was used as follows [9,26]:

$$N_s' = \frac{\dot{S}_{gen} t_{in}}{P_e} \tag{24}$$

Entransy dissipation is the loss of heat transfer potential during the heat transfer process and can be used to evaluate its irreversibility [9,14]. The entransy dissipation resulting from airflow friction is calculated as [27]:

$$\dot{E}_{\Delta p} = \frac{M_s \Delta p}{\rho} \frac{t_{out} - t_{in}}{\ln(t_{out}/t_{in})} \tag{25}$$

The entransy dissipation rate with finite temperature difference is written as [14]:

$$\dot{E}_{\Delta T} = \frac{1}{2} M_s c_p \left(t_{out}^2 - t_{in}^2\right) \tag{26}$$

The overall entransy dissipation rate is:

$$\dot{E} = \dot{E}_{\Delta p} + \dot{E}_{\Delta T} \tag{27}$$

Based on the entransy dissipation rate, Guo [28] expressed the equivalent thermal resistance as:

$$R_{ex} = \frac{\dot{E}}{P_e^2} \tag{28}$$

The dimensionless entransy dissipation rate-based thermal resistance (R^*) is [9,14]:

$$R^* = R_{ex} M_s c_p \tag{29}$$

The irreversibility and effectiveness of the downhole heater are reflected by the values of R^*. Additionally, Equations (28) and (29) cannot be used in the phase change heat transfer process without any changes.

2.5. Experimental Uncertainty

The experimental uncertainty of this work was obtained by the following equation [29,30]:

$$W_R = \sqrt{\left(\frac{\partial R}{\partial X_1} W_{x_1}\right)^2 + \left(\frac{\partial R}{\partial X_2} W_{x_2}\right)^2 \ldots\ldots + \left(\frac{\partial R}{\partial X_n} W_{x_n}\right)^2} \tag{30}$$

where $W_R = f(x_1, x_2, \ldots, x_n)$, and x_n is a variable that affects R.

In this work, the relative uncertainties of the directly measured parameters and heat transfer factor (j), heat transfer coefficient (h.t.c.) (K), friction factor (f), and pressure drop, are given in Table 3.

Table 3. Experimental uncertainties.

Uncertainty Item	Symbol	Unit	Value
Actual power	W_{P_a}	%	±(1.00–1.25)
Mass flow rate	W_{M_s}	%	±(0.16–0.24)
Surface temperature	W_T	%	±(0.23–0.26)
Inlet temperature	$W_{T_{in}}$	%	±(0.16–0.21)
Outlet temperature	$W_{T_{out}}$	%	±(0.15–0.18)
Heat transfer coefficient	W_K	%	±(3.68–5.71)
Heat transfer factor	W_j	%	±(2.05–2.63)
Pressure drop	$W_{\Delta P}$	%	±(0.15–0.19)
Friction factor	W_f	%	±(2.17–2.59)

3. Results and Discussion

All heaters were tested with identical parameters, except helical pitch values. Packer position, mass flow rate (M_s), actual power (P_a), and helical pitch value, were independent variables used to study the effects of the external air temperature of the heater shell on its performance.

The average value of each physical quantity was used to explore the heating rod temperature, characteristics of resistance and heat transfer, and total cost under a single factor, except number (N_s') and thermal resistance (R^*).

In Figures 5–14, the curves in red and the suffix "−1 (outlet)" indicate that the packer is placed at the heater outlet (Figure 1), while the curves in black and the suffix "−2 (inlet)" indicate that the packer is placed at the heater inlet (Figure 2).

3.1. Heating rod Surface Temperature

The electric heating rod surface temperature is related to the operational stability of the DEHCHB. Therefore, heating parameters for oil shale in situ pyrolysis can be improved by studying the heating rod temperature distribution trend and the influence of different packer locations on average surface temperature. Figure 5 depicts the heating rod temperature (T) along the x axis. It can be seen that the T values of all heaters in Figure 2 are higher than those in Figure 1. Moreover, in the fully developed section of helical flow, surface temperatures of H50-2, H160-2, and H210-2 are 11.59–17.92%, 19.92–28.10%, and 14.31–26.96% higher than those in Figure 1, respectively. In the fully developed shell-side section, air flow is stable helical flow and air is gradually heated; therefore, the heat transfer temperature difference is decreased, which results in T increasing linearly. Furthermore, in the two schemes, H50 has the lowest surface temperature (20.36–49.56% lower than H210, which has the highest).

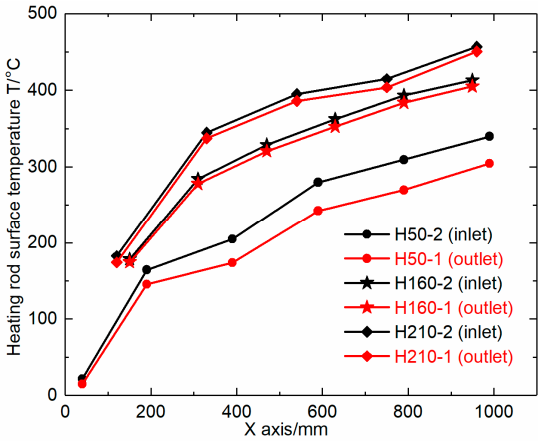

Figure 5. Heating rod surface temperature (T) with respect to x axis.

The average heating rod temperature (T_{avg}) versus mass flow rate and actual power, are shown in Figure 6. Obviously, the T_{avg} of the heater in Figure 2 is higher than that in Figure 1. The reason for this result is that the heater shell is surrounded by hot air in Figure 2. Therefore, the heat transfer driving force of the heater is lower than that in Figure 1, due to the higher air temperature and viscosity. The T_{avg} ranking for all schemes is H210 > H160 > H50; T_{avg} of H210 is 1.93–2.00 times that of H50. The greater the helical pitch, the greater the variation rate of T_{avg}. The reasons can be explained as follows: Under the given conditions, the larger the helical pitch or the smaller the mass flow, the lower the heat transfer driving force resulting from the reduced shell-side air velocity gradient. Moreover, T_{avg} increases with heating power, which is contrary to the trend of mass flow rate. That is because, as power increases, the increment in heat transfer temperature difference is not proportional to the heat absorbed by the shell-side air.

According to the T variation trend and Equations (1)–(12), in the heating process of oil shale in situ pyrolysis, the highest temperature of the heating rod can be obtained without a heating rod temperature sensor to ensure stable operation of the downhole heater. This discovery helps to reduce the difficulty in packer production.

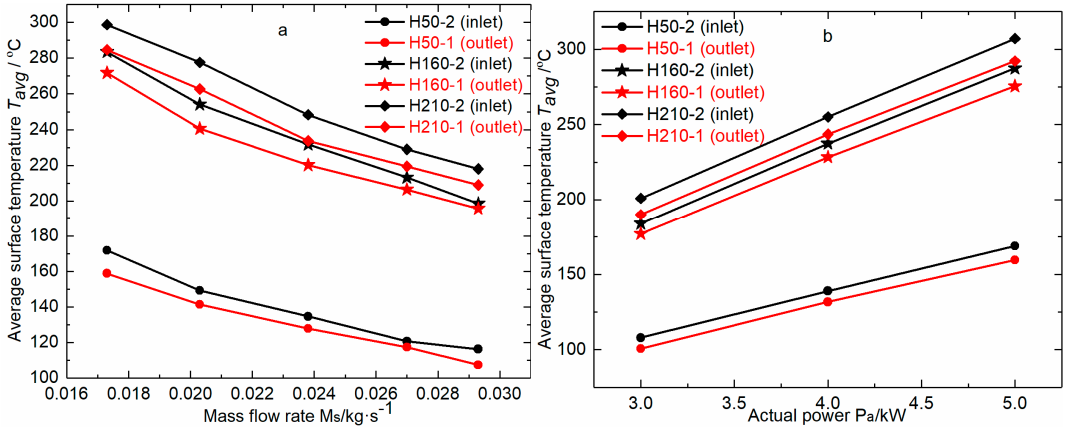

Figure 6. Average heating rod surface temperature versus (**a**) mass flow rate and (**b**) actual power.

3.2. Outlet Temperature Response Characteristics

The downhole heater was developed for igniting oil shale underground, and supplementing heat when oil shale formation heat is insufficient. The ignition temperature and burnout temperature of oil shale and oil yield of oil shale blocks are influenced by the heating rate of the downhole electric heater, which also reflect the enhanced heat transfer capability of the downhole heater [23,24]. To quickly ignite oil shale and convert kerogen into more oil, it is essential to explore the effects of the packer on the heating rate to acquire an optimal heating control strategy for the downhole heater.

Figure 7 plots the outlet temperature response curve of H50. Obviously, the outlet temperature increases rapidly in the initial stage, while its growth rate decreases in the second stage, and remains steady in final stage. The duration of each stage is related to helical pitch values, heating power, and mass flow rate. In addition, it can be clearly seen that, in the initial stage, outlet temperature of H50 in Figure 1 is higher than that in Figure 2, while the trend reverses in the second stage. Figure 8 shows the heating rate of H50 in Figure 2, versus mass flow rate and heating power. In Figure 8a, the heating rate decreases, because the amount of heat absorbed is not proportional to the increased mass flow rate. By contrast, in Figure 8b, because the heat transfer temperature difference increases with increased heating power, the heating rate increases.

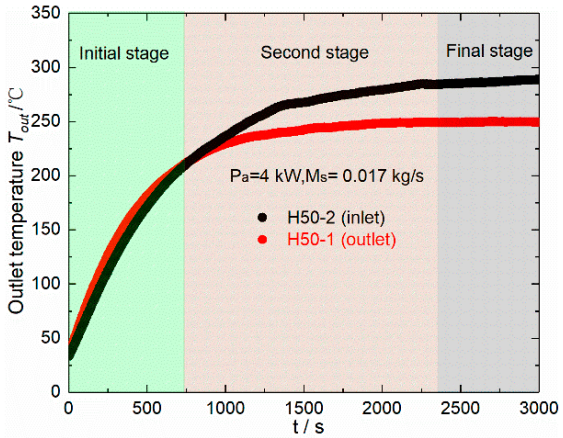

Figure 7. Outlet temperature response curve of H50.

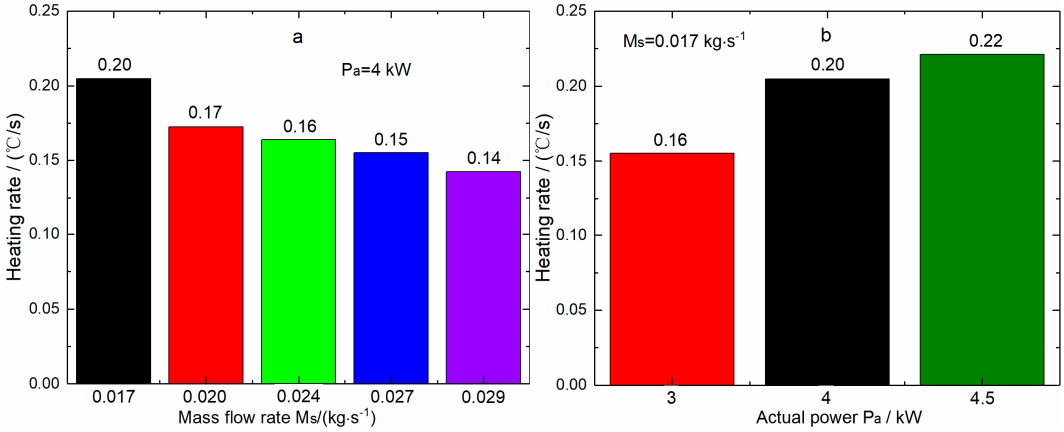

Figure 8. Heating rate versus (**a**) mass flow rate and (**b**) heating power.

3.3. Heat Transfer Performance

Figure 9 shows the variation of heat transfer coefficient (h.t.c.) (K) with respect to mass flow rate and heat transfer factor (j) as a function of the fitted Reynolds number curve. Obviously, the K and heat transfer factor of the heater in Figure 1 are larger than in Figure 2; and the smaller the pitch, the larger the difference. The reason for this result is because the shell-side air in Figure 2 can absorb extra heat from the outside of the heater shell; therefore, shell-side air temperature and viscosity in Figure 2 are higher than in Figure 1. That is, the heat transfer driving force of the heater in Figure 2 is reduced. In addition, the smaller the pitch, the more heat is absorbed by shell-side air from the outside of the heater shell. This contributes to the heat transfer temperature difference and velocity gradient of the air varying at a large rate. When M_s is 0.029 kg/s, the K of H50 is 12.79 times larger than that of H210. The general trends of K and j are also presented in Figure 7, which are H50 > H160 > H210. This is because the smaller the pitch or the larger the mass flow rate, the more heat is absorbed by the air from the heating rod for the large velocity gradient and fast separation speed. Furthermore, the heat transfer factor in Figure 2 increases monotonously with the increasing Reynolds number. In Figure 1, the j of H160 and H210 exhibit a slow decrease, whereas that of H50 increases.

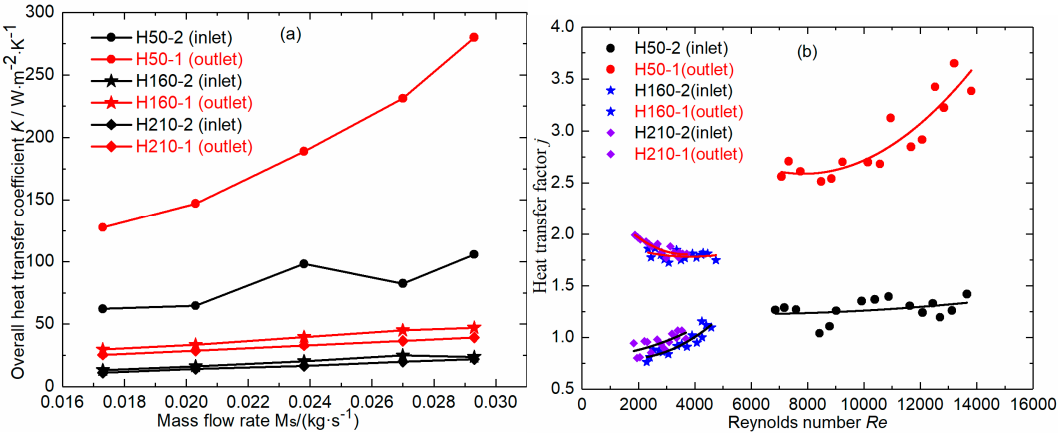

Figure 9. Heat transfer performance versus (**a**) mass flow rate and (**b**) reynolds number.

3.4. Resistance Performance

Figure 10 illustrates the variation in pressure drop with respect to the mass flow rate, and the friction factor as a function of the fitted Reynolds number curve. Clearly, the mass flow rate accelerates the pressure drop; while the variation behavior of the friction factor with respect to the Reynolds number, is the opposite. The pressure drop and friction factor of the heater in Figure 2 are larger than

those in Figure 1. The reasons for the results are as follows: The pressure drop of the heater was due to shell-side frictional resistance and local differential pressure resistance, which was the major reason. Due to the abrupt change of the airflow cross-section area, local pressure difference resistance between the leeward side of the heating rod and the inlet and outlet of the heater increases. In addition, the viscosity of air in Figure 2 is higher than in Figure 1. Thus, the local differential pressure resistance and shell-side frictional resistance increase. Beyond that, H50 exhibits the largest velocity gradient, owing to its smallest helical pitch. Therefore, H50 exhibits the largest pressure drop.

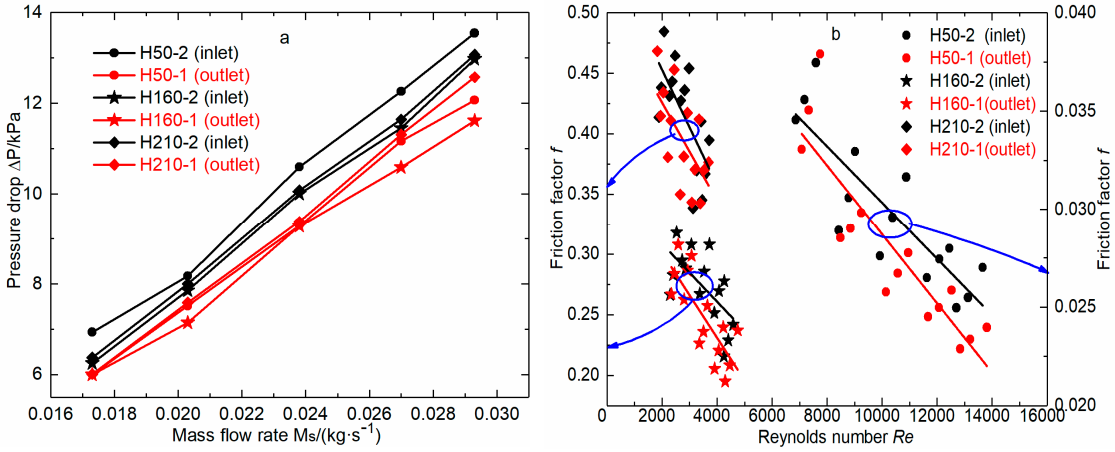

Figure 10. The resistance performance versus (**a**) mass flow rate and (**b**) Reynolds number.

3.5. Comprehensive Performance

The heat transfer performance, resistance performance, and heating rod surface temperature of the heater are synergistic; and the synergistic level is reflected by the comprehensive performance index. Therefore, a proper comprehensive index is important for investigating the effects of the packer location on the comprehensive performance of the downhole heater. In the present work, two comprehensive indices were adopted to evaluate the effect of the packer position on heater performance.

Figure 11 shows the variation trends of comprehensive performance indices, $K/\Delta P^{\frac{1}{3}}$ and $j/f^{\frac{1}{3}}$, with respect to the mass flow rate. It can be clearly seen that the comprehensive performance index increases with increasing mass flow rate. The smaller the pitch, the greater the variation rate of the comprehensive performance index. The comprehensive performance index of the heater in Figure 1 is higher than that in Figure 2. The difference between the two schemes becomes larger with decreasing pitch value or increasing mass flow rate. When M_s = 0.029 kg/s, the comprehensive performance indices of H50-1, H160-1, and H210-1 were 2.75, 2.21, and 1.87 times that of H50-2, H160-2, and H210-2, respectively. The ranking of the comprehensive performance indices are H50 > H160 > H210.

In the early stage of oil shale pyrolysis (<200 °C), the heat of the oil shale layer is mainly used to evaporate the interbedded and adsorbed water of clay minerals [31–34]. To shorten the time of oil shale dehydration, heater H50 is the best choice for heating an oil shale reservoir in the preheating stage.

3.6. Economic Analysis

Figure 12 depicts total cost versus mass flow rate and actual power. In Figure 12, total cost increases linearly with actual power, while its growth rate increases gradually with mass flow rate. Compared with Figure 2, the total cost of H50, H160, and H210 in Figure 1 was 2.91–7.58%, 3.75–9.78%, and 1.26–8.45% lower, respectively. In Figure 1, the total cost of H50 and H160 was 3.54% and 5.51% lower, respectively, than that of H210 when M_s = 0.029 kg/s; and 1.36% and 1.59% lower than that of H210 when P_a = 5 kW, respectively.

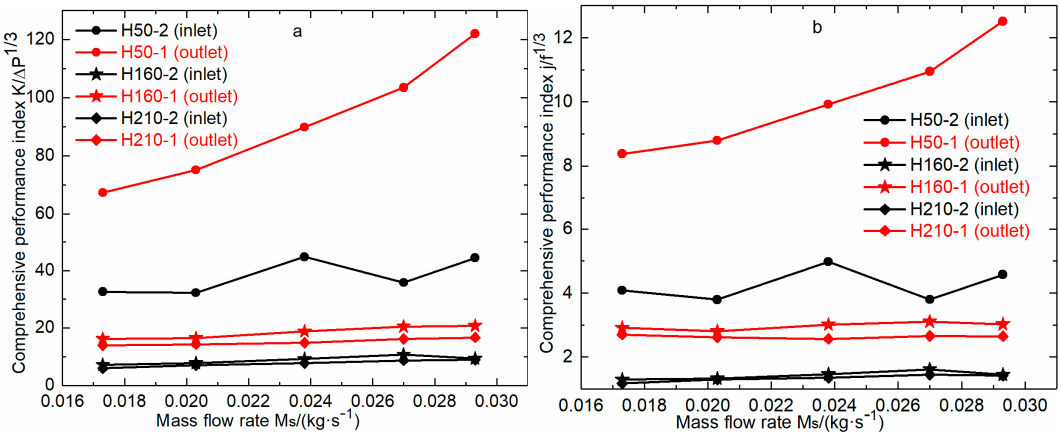

Figure 11. (**a**) comprehensive performance index $K/\Delta P^{\frac{1}{3}}$ versus mass flow rate (**b**) comprehensive performance index $j/f^{\frac{1}{3}}$ versus mass flow rate.

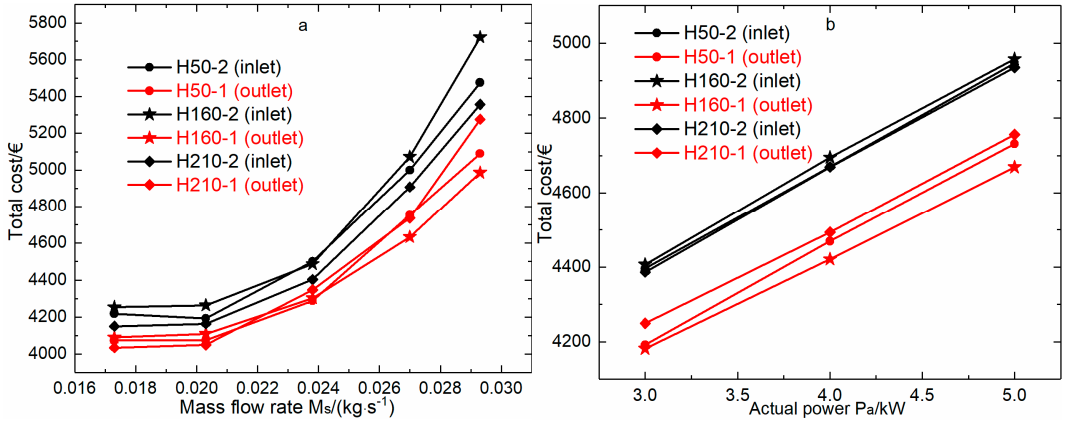

Figure 12. The total cost versus (**a**) mass flow rate and (**b**) actual power.

3.7. Performance Evaluation Based on the Second Law of Thermodynamics

In the heat transfer process, irreversibility can be reflected by entropy generation. In Figures 13 and 14, all the fitting curves show quadratic fitting. The fitted curve of the modified entropy generation rate as a function of the Reynolds number, is presented in Figure 13. It can be seen that the modified entropy generation rate (N_s') of H50-2 is greater than that of H50-1, and the difference between them increases with the increase of the Reynolds number. This is because the enhanced shell-side heat transfer capacity of H50 in Figure 1 is greater than that in Figure 2, and when the Reynolds number increases, the difference of heat transfer enhancement ability between the two schemes becomes more obvious. Additionally, H160 and H210 have similar trends due to their similar airflow cross-sectional areas. Moreover, the N_s' of H160 and H210 decreases initially and increases afterwards, in Figure 1. The variation trends of H160 and H210 in Figure 2 show the opposite behavior. Further, the variation rate of H210 is greater than that of H160. H50 exhibits the smallest modified entropy generation. The lowest N_s' of H50 indicates that H50 is more efficient than the others.

Figure 14 presents fitted curves of dimensionless entransy dissipation-based thermal resistance as a function of the Reynolds number, and a partial enlarged view of H160-1 and H210-1 are presented at the bottom. In Figure 12, H160 and H210 have similar trends. In Figure 1, the thermal resistance R^* of H160 and H210 increases initially and then decreases. The opposite trend can be observed in Figure 2. The variation rate of H210 is the largest. Based on the explanations in Sections 3.3 and 3.4, the air density of the heater in Figure 2 is higher than that in Figure 1, which results in a large equivalent velocity gradient; therefore, in a high Reynolds number region, the irreversible loss of the heater in

Figure 1 is lower than that in Figure 2. According to the second law of thermodynamics, H50 is more effective in a high Reynolds number region, than H160 and H210.

According to Figures 9–14, different packer positions not only result in different performance and total cost of the heater, but also contribute to different irreversible losses. The heater with a packer at its outlet is the optimal scheme for oil shale exploitation, as it showed the highest performance and lowest total cost.

In the second stage of oil shale pyrolysis (300–550 °C), kerogen is converted into oil. In the third stage (>600 °C), carbonate and clay minerals decompose [31–34]. To make full use of the heat injected into an oil shale formation and produce more oil, the heater H50 with a packer at its outlet should be selected to maintain the oil shale in the second stage of pyrolysis.

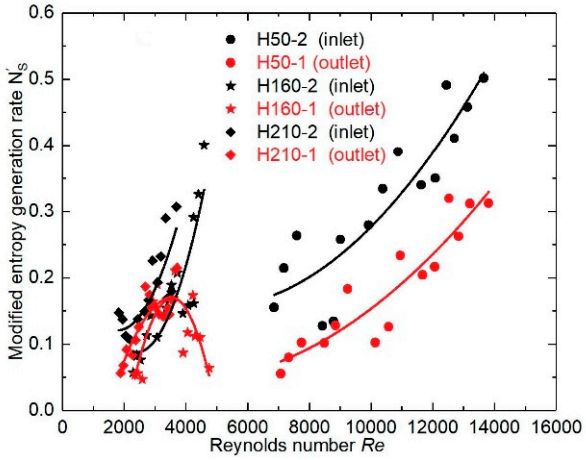

Figure 13. Modified entropy generation rate (N_s') versus Reynolds number (R_e).

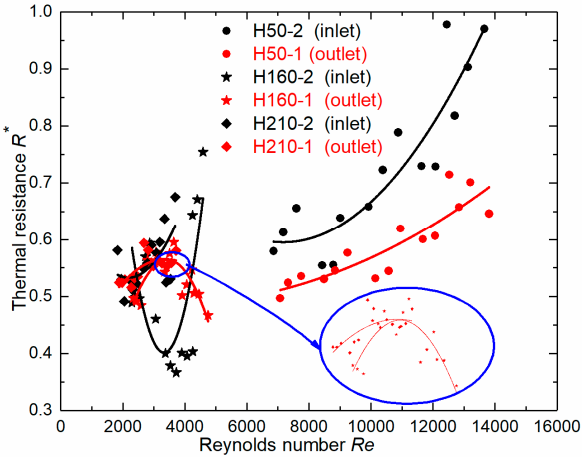

Figure 14. Dimensionless entransy dissipation rate-based thermal resistance R^* versus Reynolds number R_e

4. Conclusions

This paper investigated the effects of packer location on performance, total cost, and irreversibility by simulating the external conditions of a heater shell at different packer locations and found the optimal working scheme for the downhole heater. The following conclusions can be drawn:

(1) The surface temperature of the heater with the packer at its outlet was 11.59–26.96% lower than that of the heater in Figure 2. In addition, the heater with the packer at its outlet had an accelerated heating rate in the initial stage, and decreased temperature in the final stage.

(2) Depending on the two comprehensive performance indices, the performance of the heater with the packer at its outlet was 1.87–2.75 times that of the heater in Figure 2.

(3) Based on the second law of thermodynamics, the irreversible loss of the heater in Figure 1 is lower than that in Figure 2, with high Reynolds numbers. Compared with H160 and H210, H50 had the lowest irreversible loss of the two schemes.

(4) Regarding the comprehensive performance, total cost, and irreversible loss, H50 with the packer at its outlet is the best scheme to exploit deep oil shale resources for energy-efficient oil production.

Author Contributions: Conceptualization, Z.W.; Methodology, W.G., Z.W. and Y.S.; Software, X.L.; validation, Z.W. and Q.L.; Formal Analysis, W.G. and Z.W.; Investigation, S.D. and Y.W.; Resources, Z.W.; data Curation, Z.W. and W.G.; Writing-Original Draft Preparation, Z.W.; Writing-Review & Editing, Z.W.; Visualization, Z.W. and Q.L.; Supervision, Z.W. and Q.L. All authors have read and agreed to the published version of the manuscript.

Funding: This research was funded by the National Key R&D Program of China (Grant No. 2019YFA0705502, Grant No. 2019YFA0705501), the Project of Jilin Province Development and Reform Commission of China, the Cooperative Project between Universities and Jilin Province, China (Grant No. SF2017-5-1), the Program for JLU Science and Technology Innovative Research Team (Grant No. 2017TD-13), and the Fundamental Research Funds for the Central Universities.

Conflicts of Interest: The authors declare no conflict of interest.

Nomenclature

A	Heat transfer area: m^2
d_e	Hydraulic diameter, m
$\dot{E}$	Entransy dissipation rate, W/K
h	Convective heat transfer coefficient, $W{\cdot}m^{-2}{\cdot}K^{-1}$
K	Overall heat transfer coefficient, $W{\cdot}m^{-2}{\cdot}K^{-1}$
M_s	Mass flow rate, kg/s
N_s'	Modified entropy generation number
N_u	Nusselt number
P_a	Actual power, W
P_e	Effective power, W
P_r	Prandlt number
R_e	Reynolds number
R_{ex}	Equivalent thermal resistance, K/W
f	Friction factor
j	Heat transfer factor
$\dot{S}_{gen}$	Entropy generation rate, W/K
T	Heating rod temperature, K
T_{avg}	Average heating rod surface temperature, K
T_{in}	The inlet air temperature, K
Greek symbols	
λ	Thermal conductivity, W/(m k)
ΔP	Pressure drop, Pa
ρ	Density, kg/m^3
μ	Dynamic viscosity, $kg{\cdot}m^{-1}s^{-1}$
Δt_m	Logarithmic heat transfer temperature difference, K
Δt_{max}	Maximum temperature difference, K
Δt_{min}	Minimum temperature difference, K
Subscripts	
in	inlet or inner
out	outlet or outer
s	shell-side

References

1. Shen, F.; Cheng, L.; Sun, Q.; Huang, S. Evaluation of the Vertical Producing Degree of Commingled Production via Waterflooding for Multilayer Offshore Heavy Oil Reservoirs. *Energies* **2018**, *11*, 2428. [CrossRef]
2. Lu, T.; Li, Z.; Zhou, Y. Flow Behavior and Displacement Mechanisms of Nanoparticle Stabilized Foam Flooding for Enhanced Heavy Oil Recovery. *Energies* **2017**, *10*, 560.
3. Wang, L.; Yang, D.; Li, X.; Zhao, J.; Wang, G.; Zhao, Y. Macro and Meso Characteristics of In-Situ Oil Shale Pyrolysis Using Superheated Steam. *Energies* **2018**, *11*, 2297. [CrossRef]
4. Zhou, X.; Yuan, Q.; Zhang, Y.; Wang, H.; Zeng, F.; Zhang, L. Performance evaluation of CO_2 flooding process in tight oil reservoir via experimental and numerical simulation studies. *Fuel* **2019**, *236*, 730–746. [CrossRef]
5. Sun, Y.; Liu, Z.; Li, Q.; Deng, S.; Guo, W. Controlling groundwater infiltration by gas flooding for oil shale in situ pyrolysis exploitation. *J. Pet. Sci. Eng.* **2019**, *179*, 444–454. [CrossRef]
6. Saif, T.; Lin, Q.; Gao, Y.; Al-Khulaifi, Y.; Marone, F.; Hollis, D.; Blunt, M.J.; Bijeljic, B. 4D in situ synchrotron X-ray tomographic microscopy and laser-based heating study of oil shale pyrolysis. *Appl. Energy* **2019**, *235*, 1468–1475. [CrossRef]
7. Guo, W.; Wang, Z.; Sun, Z.; Sun, Y.; Lü, X.; Deng, S.; Qu, L.; Yuan, W.; Li, Q. Experimental investigation on performance of downhole electric heaters with continuous helical baffles used in oil shale in-situ pyrolysis. *Appl. Therm. Eng.* **2019**, *147*, 1024–1035. [CrossRef]
8. Wu, Z.; Liu, H. Investigation of hot-water flooding after steam injection to improve oil recovery in thin heavy-oil reservoir. *J. Pet. Explor. Prod. Technol.* **2019**, *9*, 1547–1554. [CrossRef]
9. Huang, S.; Chen, X.; Liu, H.; Xia, Y.; Jiang, J.; Cao, M.; Li, A.; Yang, M. Experimental and numerical study of steam-chamber evolution during solvent-enhanced steam flooding in thin heavy-oil reservoirs. *J. Pet. Sci. Eng.* **2019**, *172*, 776–786. [CrossRef]
10. Du, T.; Chen, Q.; Du, W.; Cheng, L. Performance of continuous helical baffled heat exchanger with varying elliptical tube layouts. *Int. J. Heat Mass Transf.* **2019**, *133*, 1165–1175. [CrossRef]
11. Yadav, S.; Sahu, S.K. Effect of Helical Surface Disc Turbulators on Heat Transfer and Friction Factor Characteristics in the Annuli of a Double-Pipe Heat Exchanger. *Chem. Eng. Technol.* **2019**, *42*, 1205–1213. [CrossRef]
12. Gu, X.; Luo, Y.; Xiong, X.; Wang, K.; Wang, Y. Numerical and experimental investigation of the heat exchanger with trapezoidal baffle. *Int. J. Heat Mass Transf.* **2018**, *127*, 598–606. [CrossRef]
13. Wang, X.; Zheng, N.; Liu, P.; Liu, Z.; Liu, W. Numerical investigation of shell side performance of a double shell side rod baffle heat exchanger. *Int. J. Heat Mass Transf.* **2017**, *108*, 2029–2039. [CrossRef]
14. Gao, B.; Bi, Q.; Nie, Z.; Wu, J. Experimental study of effects of baffle helix angle on shell-side performance of shell-and-tube heat exchangers with discontinuous helical baffles. *Exp. Therm. Fluid Sci.* **2015**, *68*, 48–57. [CrossRef]
15. Stehlik, P.; Němčanský, J.; Kral, D.; Swanson, L.W. Comparison of Correction Factors for Shell-and-Tube Heat Exchangers with Segmental or Helical Baffles. *Heat Transf. Eng.* **1994**, *15*, 55–65. [CrossRef]
16. Boukhadia, K.; Ameur, H.; Sahel, D.; Bozit, M. Effect of the perforation design on the fluid flow and heat transfer characteristics of a plate fin heat exchanger. *Int. J. Therm. Sci.* **2018**, *126*, 172–180. [CrossRef]
17. Churchill, S.W.; Bernstein, M. A correlating equation for forced convection from gases and liquids to a circular cylinder in crossflow. *J. Heat Transf.* **1977**, *99*, 300–306. [CrossRef]
18. Wu, J.; Zhou, J.; Chen, Y.; Wang, M.; Dong, C.; Guo, Y. Experimental investigation on enhanced heat transfer of vertical condensers with trisection helical baffles. *Energy Convers. Manag.* **2016**, *109*, 51–62. [CrossRef]
19. Shah, R.K.; Sekulić, D.P. *Fundamentals of Heat Exchanger Design*; John Wiley & Sons: New York, NY, USA, 2003.
20. Taal, M.; Bulatov, I.; Klemeš, J.; Stehlík, P. Cost estimation and energy price forecasts for economic evaluation of retrofit projects. *Appl. Therm. Eng.* **2003**, *23*, 1819–1835. [CrossRef]
21. Wang, K.; Cheng, L. Numerical modeling and multi-objective optimization of a novel cross-flow heat exchanger with rotated aligned tube bank. *Sci. China Technol. Sci.* **2018**, *61*, 982–993. [CrossRef]
22. Li, J.; Wang, K.; Cheng, L. Experiment and optimization of a new kind once-through heat recovery steam generator (HRSG) based on analysis of exergy and economy. *Appl. Therm. Eng.* **2017**, *120*, 402–415. [CrossRef]
23. Mu, M.; Han, X.; Jiang, X. Combined fluidized bed retorting and circulating fluidized bed combustion system of oil shale: 3. Exergy analysis. *Energy* **2018**, *151*, 930–939. [CrossRef]

24. Han, X.; Niu, M.; Jiang, X. Combined fluidized bed retorting and circulating fluidized bed combustion system of oil shale: 2. Energy and economic analysis. *Energy* **2014**, *74*, 788–794. [CrossRef]
25. Chen, X.; Zhao, T.; Zhang, M.; Chen, Q. Entropy and entransy in convective heat transfer optimization: A review and perspective. *Int. J. Heat Mass Transf.* **2019**, *137*, 1191–1220. [CrossRef]
26. Liu, J.; Jiang, Y.; Wang, B.; He, S. Assessment and optimization assistance of entropy generation to air-side comprehensive performance of fin-and-flat tube heat exchanger. *Int. J. Therm. Sci.* **2019**, *138*, 61–74. [CrossRef]
27. Qian, S.; Huang, L.; Aute, V.; Hwang, Y.; Radermacher, R. Applicability of entransy dissipation based thermal resistance for design optimization of two-phase heat exchangers. *Appl. Therm. Eng.* **2013**, *55*, 140–148. [CrossRef]
28. Guo, Z.Y.; Liu, X.B.; Tao, W.Q.; Shah, R.K. Effectiveness–thermal resistance method for heat exchanger design and analysis. *Int. J. Heat Mass Transf.* **2010**, *53*, 2877–2884. [CrossRef]
29. Moffat, R.J. Describing the uncertainties in experimental results. *Exp. Therm. Fluid Sci.* **1988**, *1*, 3–17. [CrossRef]
30. Kline, S.J. Describing Uncertainties in Single-Sample Experiments. *Mech. Eng.* **1953**, *75*, 3–8.
31. Wang, S.; Jiang, X.; Han, X.; Tong, J. Investigation of Chinese oil shale resources comprehensive utilization performance. *Energy* **2012**, *42*, 224–232. [CrossRef]
32. Yan, J.W.; Jiang, X.M.; Han, X.X. Study on the Characteristics of the Oil Shale and Shale Char Mixture Pyrolysis. *Energy Fuels* **2009**, *23*, 5792–5797. [CrossRef]
33. Pan, L.; Dai, F.; Li, G.; Liu, S. A TGA/DTA-MS investigation to the influence of process conditions on the pyrolysis of Jimsar oil shale. *Energy* **2015**, *86*, 749–757. [CrossRef]
34. Cheikh Moine, E.; Groune, K.; El Hamidi, A.; Khachani, M.; Halim, M.; Arsalane, S. Multistep process kinetics of the non-isothermal pyrolysis of Moroccan Rif oil shale. *Energy* **2016**, *115*, 931–941. [CrossRef]